Sustainable Polymer & Energy

SCIEPublish

Article

Functionalized Polyurethane as a Hole Transport Layer for Quantum Dot-Sensitized Solar Cells with Higher Open-Circuit Voltage and Fill Factor

Upakar Patel, Shubham Kumar, Alok Kumar, Anupama Devi and Pralay Maiti *

School of Materials Science and Technology, Indian Institute of Technology (Banaras Hindu University), Varanasi 221005, India; upakarpatel.rs.mst23@itbhu.ac.in (U.P.); shubhamkumar.mst24@itbhu.ac.in (S.K.); alokkumar.rs.mst23@itbhu.ac.in (A.K.); anupamadevi.rs.mst23@itbhu.ac.in (A.D.)

* Corresponding author. E-mail: pmaiti.mst@itbhu.ac.in (P.M.)

Received: 9 July 2026; Revised: 22 July 2026; Accepted: 12 August 2026; Available online: 27 August 2026

ABSTRACT: A functionalized polyurethane-based hole transport layer (HTL) for quantum dot-sensitized solar cells (QDSSCs) has been developed by tailoring the redox behaviour of segmented polyurethane. The successful incorporation of ionic moieties into the hard segment was confirmed by Fourier-transform infrared (FTIR) and Nuclear magnetic resonance (NMR) spectroscopy. Sulfonation significantly improved the polymer's electrical conductivity, electrochemical activity, and optical properties, thereby enabling efficient hole transport through favorable work-function alignment and reduced interfacial energy barriers between the photoactive layer and the Ag counter electrode. Ultrasmall spherical $CuInS_2$ quantum dots with an average size of 3.15 nm were synthesized using a capping-assisted method and characterized by X-ray diffraction (XRD), UV-Vis spectroscopy, and Transmission electron microscopy (TEM). The HOMO-LUMO and valence/conduction band energy levels, determined by cyclic voltammetry and UV-vis spectroscopy, revealed favorable energy level alignment for efficient charge separation and hole extraction. QDSSCs were fabricated with the architectures FTO/TiO_2/$CuInS_2$/SPU-2/Ag and FTO/SnO_2/TiO_2/$CuInS_2$/SPU-2/Ag. The introduction of an SnO_2 interfacial electron transport layer enhanced electron extraction by improving the energy band alignment with TiO_2, resulting in an increase in photocurrent density from 0.74 to 2.12 $mA \cdot cm^{-2}$. The corresponding devices exhibited high open-circuit voltages of 0.89 and 0.75 V, fill factors of 67% and 56%, and power conversion efficiencies of 0.45% and 0.89%, respectively. These results demonstrate that the functionalized polyurethane HTL, combined with a SnO_2/TiO_2 bilayer electron transport layer (ETL), provides an effective strategy to improve charge transport and enhance the photovoltaic performance of $CuInS_2$-based QDSSCs.

Keywords: QDSSCs; $CuInS_2$; HTL; ETL; Polyurethane

1. Introduction

Due to their special optical and electrical characteristics, quantum dots, also known as semiconductor nanocrystals (diameter of 2–10 nm), are a novel class of materials that have drawn the attention of most researchers worldwide during the past ten years [1]. High quantum yields, size-dependent band gaps, multiple exciton generation, hot electron transfer, high extinction coefficients, and photostability are all present. These special qualities make it a viable substitute for organic chromophores in a variety of applications, including biomedical imaging, photovoltaics, and light-emitting diodes. Due to their superior optoelectronic qualities, conventional quantum dots such as CdS, CdSe, CdTe, PbS, PbSe, SnS, and SnSe have been extensively used in photovoltaics [2,3]. However, many of these materials contain potentially dangerous elements, especially lead (Pb) and cadmium (Cd), which limit their widespread commercialization and raise serious health and environmental concerns. The International Agency for Cancer Research (IARC) classified cadmium and lead as type I carcinogens. These materials can cause tumors in the lungs, prostate, injection site, and other tissues [4,5]. A potential inorganic semiconductor made of elements that are generally safe for the environment, copper indium sulfide ($CuInS_2$), is a desirable substitute for traditional heavy-metal-based quantum dots. Due to its exceptional photoelectric properties, which include a high optical absorption coefficient ($>10^4$ cm^{-1}), an appropriate optical band gap (1.5 eV), excellent radiation stability, and remarkable defect tolerance, it has drawn a lot of attention in recent years for photovoltaic and optoelectronic applications. $CuInS_2$ is an excellent material for next-generation solar energy conversion technologies because of its inherent properties, which enable effective light harvesting, enhanced charge-carrier generation, and stable device performance [6–8]. Copper indium sulfide ($CuInS_2$) QDs have a high absorption coefficient, a tunable band gap, and are non-toxic, environmentally friendly chalcopyrite semiconducting materials [9]. According to the Shockley-Queisser limit, a $CuInS_2$-based solar cell could potentially have a power conversion efficiency of 30–32% [6,10]. Although $CuInS_2$ has poor electrochemical catalytic properties, high recombination of photogenerated electron-hole pairs and low photochemical stability still limit its photoelectrocatalytic and electrocatalytic performance, despite improvements based on the aforementioned studies [11].

The performance of QDSSCs is directly affected by electrolyte behaviour. Lately, liquid electrolytes like I^-/I_3^- and S^{-2}/S_n^{-2} electrolytes have been widely used in QDSSCs. To complete the circuit and generate an electric current, the electrolyte mediator accepted the hole and shifted it to the counter electrode. Leakage is an issue for QDSSCs that use liquid electrolytes [12]. To solve this problem, we need to develop a different physical form of electrolytes, like semi-solid gel electrolytes or solid film. This is required because ordinary liquid electrolytes have poor long-term stability, are difficult to handle, and are prone to evaporation. Numerous research teams have created QDSSC devices using solid-state and semi-solid (gel form) polymer electrolytes [13–15]. The polyurethane (PU) is usually used as a matrix for the preparation of gel. Pure PU is an insulator, but you can improve its electrical conductivity by adding polar groups, like sulfonate moieties, to the polymer chain. This makes conduction easier. Besides its electrical conductivity, its good mechanical properties and long-term stability make it a good choice as a hole-transporting material [15]. By adding sulfonic acid ($–SO_3H$) groups to the polyurethane backbone, sulphonation greatly improves its physicochemical characteristics. These functional groups boost ionic conductivity, hydrophilicity, and adhesion to metal oxide photoanodes like TiO_2 and SnO_2. Furthermore, by interacting strongly with the surfaces of semiconductor quantum dots like $CuInS_2$, CdS, and CdSe, the $–SO_3H$ groups successfully passivate surface defects that act as charge recombination centers. This interfacial passivation can increase the open-circuit voltage (V_{OC}) and fill factor (FF) of QDSSCs while also inhibiting charge recombination and promoting efficient hole extraction [16,17].

Sulphonated polyurethane (SPU) can facilitate efficient hole extraction in QDSSCs based on $CuInS_2$ quantum dots placed on TiO_2 photoanodes by establishing close interfacial contact and reducing defect-

induced charge recombination. It is a promising material for wearable and flexible solar cells on polymer substrates such as ITO-coated polyethylene terephthalate due to its exceptional flexibility and solution processability [18].

In this article, a synthesized, functionalized thermoplastic PU is used as a hole transport layer (HTL), and various semiconducting materials, such as SnO_2 and TiO_2, are used as electron transport layers (ETLs) in QDSSCs. Gel electrolyte-based QDSSCs are fabricated using FTO/TiO_2/$CuInS_2$ and FTO/SnO_2/TiO_2/$CuInS_2$ as the photoelectrode. And SPU-2 is used as a hole-transport layer due to higher ionic conductivity as compared to SPU-1, at the counter electrode. Overall, sulphonated polyurethane represents a promising emerging hole transport material for QDSSCs. Its low intrinsic conductivity remains a problem, but it can be overcome through molecular engineering, controlled sulphonation, or the creation of conductive polymer composites. SPU has great potential for use in next-generation, flexible, affordable, and eco-friendly quantum dot-sensitized solar cells, with further optimization of its energy-level alignment and charge-transport properties.

2. Experimental

2.1. Precursor Materials

4,4-diphenylmethane diisocyanate (MDI, 98%), sodium hydride (NaH, 55–65%, moistened with paraffin oil), poly(tetramethylene glycol) (PTMG, Mn = 2900 g/mol from Sigma-Aldrich, Bengluru, India), 1,3-propane sultone (≥99%, Sigma-Aldrich, Bengluru, India), butane diol (BD, Sigma-Aldrich, Bengluru, India), dibutyl tindilaurate (DBTDL, 95% from Sigma-Aldrich,Bengluru, India), N,N-dimethyl acetamide (DMAc, ≥99%), N,N-dimethylformamide (DMF, ≥99.9%), N-methyl pyrrolidone (NMP, 99.5%), Potassium Ferrocynide ($K_4[Fe(CN)_6]$, 99%), Potassium Ferricynide ($K_3[Fe(CN)_6]$, 98%), Potassium chloride (KCl), 1-Dodecanethiol (≥98%, Sigma-Aldrich, Bengluru, India), 3-mercaptopropinoic acid (3-MPA, ≥99.9%), Indium(iii) acetate ($In(OAc)_3$, 99.99% from thermoscientific, India), Copper Iodide (CuI), Dichloromethne, Methanol (CH_3OH, ≥99.8%), Acetone (CH_3COCH_3, 99.7%), Fluorine-doped tin oxide (FTO)-coated glass substrates (Sigma-Aldrich, Bengluru, India) with a thickness of 2.2 mm and a sheet resistance of 14 Ω/sq, TiO_2 paste (Solaronix, Switzerland), Anhydrous tin(II) chloride ($SnCl_2$, ≥99.9%, Sigma-Aldrich, Bengluru, India), Silver conductive paste (Elcosil S-L/SP from Solaronix, Switzerland).

2.2. Synthesis of $CuInS_2$

The one-pot synthesis method used for the synthesis of $CuInS_2$ QDs, in which 292 mg of Indium acetate and 190 mg of copper iodide were taken in a round-bottom flask, mixed with 7.5 mL of 1-dodecanethiol. The reaction mixture was purged with nitrogen gas three to four times to establish an inert N_2 atmosphere. Under strong stirring, the temperature was raised to 100 °C until a light yellow solution formed, then increased to 210 °C. As the temperature rose to 210 °C, the color of the reaction mixture changed from yellow to light red, then to dark red, addressing the $CuInS_2$ QDs nucleation and growth. To quickly stop further nanoparticle growth, the reaction mixture was rapidly cooled to below 50 °C. The resulting QDs were washed several times by centrifugation at 7000 RPM in a mixture of excess methanol and 0.1 M 3-mercaptopropionic acid (3-MPA) to eliminate unreacted precursor [19,20]. The aim of using 3-MPA is, to surface passivate defect states, enhance colloidal stability, and facilitate efficient charge transfer between the $CuInS_2$ quantum dots and the TiO_2 photoanode, thereby improving QDSSC performance [21].

2.3. Synthesis of PU

A two-step condensation polymerization method was used to make the MDI-based polyurethane (PU). In the first step, an isocyanate-terminated prepolymer was prepared by reacting 1.3 g of poly(tetramethylene glycol) (PTMG) with 0.8 g of 4,4′-methylene diphenyl diisocyanate (MDI) in 20 mL DMF. This reaction

was carried out under continuous stirring at 70 °C for 3 h in an inert atmosphere. Subsequently, 0.2 mL butane diol was introduced as a chain extender, followed by the addition of a catalyst (1 mL of 1% DBTDL in toluene). The reaction mixture was stirred continuously at the same temperature under an inert atmosphere for 24 h. The cold deionized water is used to precipitate the resulting polyurethane. The collected precipitate was dried first on a hot plate, then in a vacuum oven at 50 °C for 72 h [22]. A schematic representation of the reaction is shown in Figure 1a.

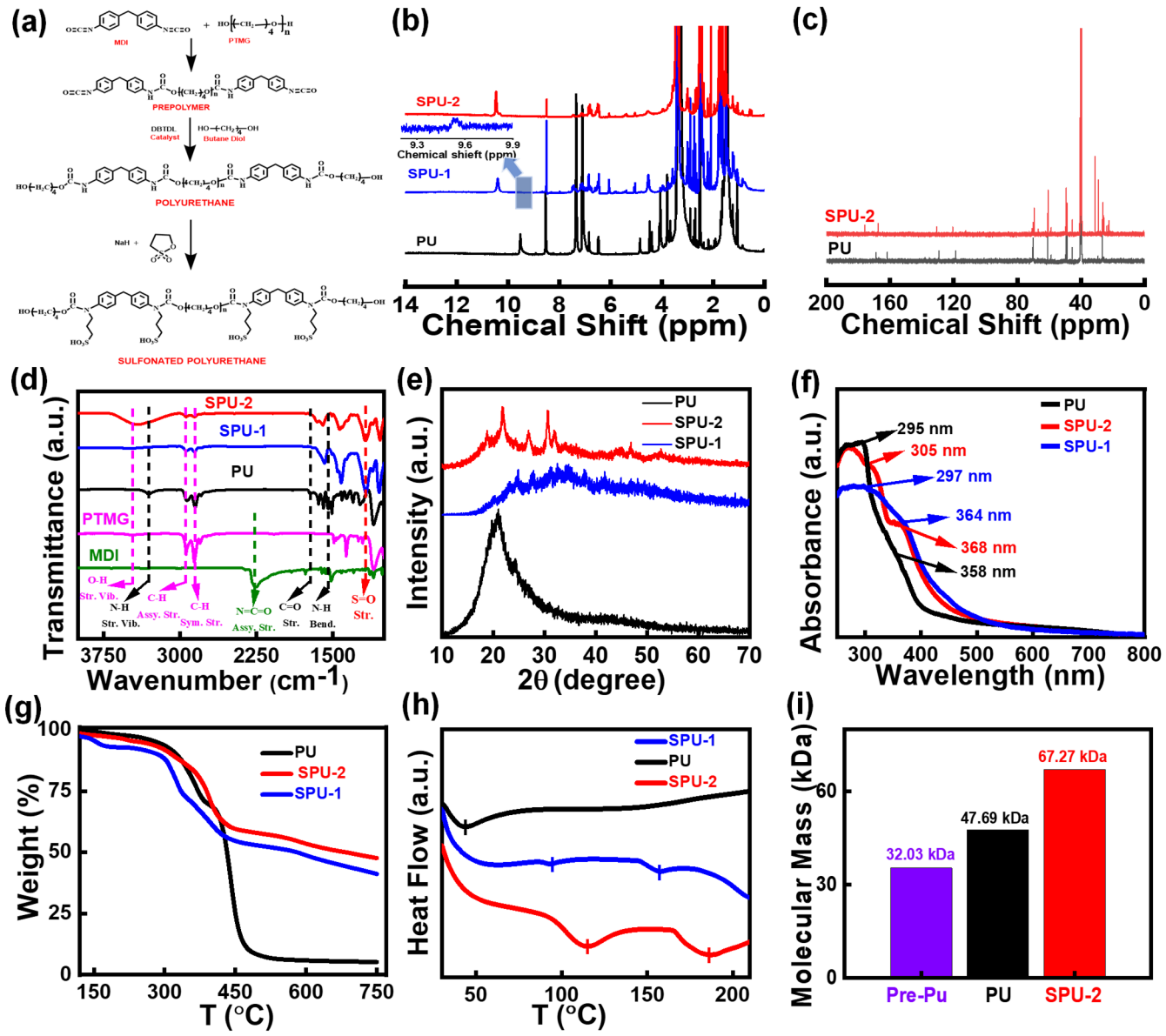

Figure 1. (**a**) Reaction scheme to synthesize butane diol extended thermoplastic polyurethane (PU) and functionalization of hard segment using propane sultone to generate ionomer (SPU-1 and SPU-2); (**b**) ^{1}H NMR spectra of pure PU, functionalized polymer SPU-1 and SPU-2; (**c**) ^{13}C NMR spectra of pure PU and SPU; (**d**) FTIR spectra of synthesized pure PU, SPU-1 and SPU-1, showing appearance of new peak and shifting of peak position; (**e**) XRD spectra of PU SPU-1 and SPU-2; (**f**) UV-vis absorption spectra of pure PU, SPU-1 and SPU-2 showing the shifting of peak position; (**g**) TGA thermograms of Pure PU, SPU-1 and SPU-2 demonstrating relative thermal stability; (**h**) DSC thermograms of pure PU, SPU-1 and SPU-2 showing the melting temperatures; and (**i**) Weight average molecular mass histogram of Pre-PU, PU and SPU-2, shows successful polymerization and sulphonation.

2.4. Functionalization of Polyurethane

A bimolecular nucleophilic substitution reaction method was used to functionalize the synthesized polyurethane. At the start of the reaction, 0.3 g of synthesized polymer was dissolved using 15 mL DMAc solvent in a round-bottom flask at 60 °C, and then the reaction temperature was taken to room temperature. Under an inert atmosphere, 0.6 g NaH was added to the solution at 0 °C with vigorous stirring, and the mixture was kept at this temperature for 1 h. After that, the reaction mixture was cooled to room temperature. After this, 0.750 mL (for SPU-1) and 1 mL (for SPU-2) 1,3-propane sultone is added, and the mixture is continuously stirred for 3 h at 65 °C. After the reaction mixture is complete, cool to room temperature, then pour it into a toluene-containing beaker to precipitate the ionomer and remove any unreacted reagents. Finally, the sulphonated PU (SPU) was collected and washed two to three times with ethanol and diethyl ether [23], as shown in Figure 1a.

2.5. Preparation Gel Electrolytes

In the DMF solvent, the functionalized polymer was added to form a semi-solid gel. Under continuous stirring, the solution was heated to 80 °C until a homogenous mixture was formed. A semi-solid ionomer (SPU) gel was formed by cooling it to 5 °C and keeping it there for 12 h.

2.6. Device Fabrication

To investigate the influence of different ETLs, QDSSCs were fabricated with identical device architectures, varying only in the ETL configuration to enable a direct comparison of their photovoltaic performance. All other functional layers and fabrication conditions were kept unchanged to ensure a reliable comparative evaluation. The fabricated devices consisted of Glass/FTO/TiO_2/$CuInS_2$/SPU-2/Ag and Glass/FTO/SnO_2/TiO_2/$CuInS_2$/SPU-2/Ag architectures, designated as Device-1 and Device-2, respectively. Device fabrication commenced with the preparation of FTO-coated glass substrates. The substrates were patterned by chemical etching with a zinc-hydrochloric acid solution to define the active area, as illustrated in Supplementary Figure S1a. Subsequently, they were cleaned sequentially in soap solution, acetone, and isopropanol (IPA), with ultrasonication applied at each step. Finally, the oxygen plasma is used for cleaned treated substrate at 20 W for 10 min to improve film adhesion. For Device-1, a TiO_2 layer is deposited by doctor-blade coating and subsequently annealed at 500 °C for 30 min (Figure S1b). And for Device-2, SnO_2 as ETL is deposited by spin coating a 500 mM solution of $SnCl_2$ at 5000 rpm for 50 s under ambient conditions. The film is then annealed at 550 °C for 30 min to yield a transparent SnO_2 layer, and the top of the SnO_2, TiO_2 layer is deposited by doctor-blade coating and subsequently annealed at 500 °C for 30 min [24]. For the coating of the active layer ($CuInS_2$), the dip coating method was used with a solution of $CuInS_2$ prepared in dichloromethane [25]. The counter electrode was prepared by using silver paste on FTO through the doctor blade coating method. After annealing at 130 °C for 15 min, we obtained a thin layer of Ag (Figure S1b). Finally, the active area of both devices is ~0.56 cm^2, and a schematic figure of the complete device architecture is presented in Figure S1c.

2.7. Characterization

2.7.1. X-ray Diffraction

The structural characteristics of the synthesized QDs, pure polymer, and functionalized polymer were examined using an X-ray diffraction instrument (Rigaku Miniflex 600, Rigaku Corporation, Tokyo, Japan) with Cu Kα radiation (λ = 0.154 nm), operated at a constant current of 15 mA and a voltage of 40 kV. The samples were mounted on a quartz holder and analyzed at ambient temperature with a scanning rate of 3° min^{-1} over a 2θ range of 10–70°.

2.7.2. Spectroscopic Measurements

The ^{1}H NMR spectra of the functionalized polymer were recorded on a Bruker Biospin spectrometer (500 MHz, Bruker, Ettlingen, Germany), and the chemical shifts were expressed in ppm. DMSO-d_6 was used as the solvent for the ^{1}H NMR measurements. All spectroscopic measurements were conducted at room temperature. For optical analysis, a JASCO V-650 UV-visible spectrophotometer (JASCO Corporation, Tokyo, Japan), was used to record the UV-Vis absorption spectra of the various polymers and the synthesized quantum dots at a scan rate of 2 nm·s^{-1}, over a wavelength range of 200–800 nm. Photoluminescence measurements were carried out in fluorescence mode using a BioTek Synergy H1 instrument (BioTek, Winooski, VT, USA). FTIR transmittance spectra of the quantum dots and polymers were obtained using a Nicolet 670 spectrometer (Thermo Fisher Scientific Inc., Madison, WI, USA.), with 100 scans at a resolution of 4 cm^{-1}, over the spectral range of 600–4000 cm^{-1}.

2.7.3. DLS and Zeta Potential

A Litesizer DLS 701 Particle Analyzer (Anton Paar, Graz, Austria) instrument was used to measure the molecular mass and zeta potential of the polymers at room temperature (25 °C). For molecular weight analysis, three different sample concentrations (0.25, 0.5, and 1 mg·mL^{-1}) of the prepolymer, polymer, and functionalized polymer were prepared. For zeta potential analysis, a 1.5 mg·mL^{-1} sample prepared in DMF was used.

2.7.4. Thermal Analysis

An instrument (Mettler-Toledo, Greifensee, Switzerland), a thermogravimetric analyzer, is used for the analysis of the thermal behavior of pristine polymer and functionalized polymer over the temperature range 30–750 °C. The thermal behaviour of the pristine polymer and its functionalized derivatives was investigated using a Mettler-Toledo thermogravimetric analyzer at a heating rate of 20 °C min^{-1} over the temperature range 30–750 °C under an inactive atmosphere. The Mettler 832 instrument is used for differential scanning calorimetry (DSC) measurements. It operates under a nitrogen atmosphere with a heating rate of 10 °C per minute and covers a temperature range of 0–300 °C.

2.7.5. Cyclic Voltammetry

An instrument, (Metrohm Autolab M204, Metrohm Autolab B.V., Utrecht, The Netherlands) is used for cyclic voltammetry measurements of the polymer, CIS QDs, and ETLs with a three-electrode setup, platinum as the counter electrode, Ag/AgCl as the reference electrode, and glassy carbon as the working electrode. The conduction band (CB) and valence band (VB) of QDs, and the highest occupied molecular orbital (HOMO) energy level and lowest unoccupied molecular orbital (LUMO) energy level of polymer, were calculated from CV measurement. Equations (1) and (2) are used to calculate the HOMO and LUMO energy levels of the polymer and QDs, reference material (−4.4 eV) ferrocene is used.

$$E_{\mathrm{HOMO}} = -\mathrm{eV}\,(E_{ox}^{onset} + 4.4) \quad (1)$$

$$E_{\mathrm{LUMO}} = -\mathrm{eV}\,(E_{red}^{onset} + 4.4) \quad (2)$$

10 mL of *N*-methyl-2-pyrrolidone (NMP) solvent is used to dissolve 5 mg of the polymers. The sample solution was prepared by mixing 5 mg of polymer, while 2 mg of $CuInS_2$ (CIS) quantum dots were dispersed in 6 mL of the same solvent. The resulting solutions were ultrasonicated for 15 min to ensure uniform dispersion. A blank cyclic voltammetry (CV) measurement was first performed using pure NMP to determine the appropriate working potential window. Subsequently, CV measurements were carried out at room temperature of the prepared sample over a potential range of −2.0 to +2.0 V at a scan rate of 20

$mV \cdot s^{-1}$. The TiO_2 and SnO_2 electron transport layers (ETLs) were deposited onto FTO substrates. The electrolyte was prepared by dissolving 5 mM ferricyanide, 5 mM ferrocyanide, and 0.1 M KCl in deionized water. Before evaluating the ETLs, a CV measurement was performed using a bare FTO electrode in the prepared electrolyte to establish the appropriate working potential window. The TiO_2 and SnO_2 ETLs were then analyzed by CV at room temperature over a potential range of −0.9 to +1.0 V at a scan rate of 20 $mV \cdot s^{-1}$ under a nitrogen atmosphere.

2.7.6. Electrochemical Impedance Spectroscopy (EIS)

The electrochemical impedance spectroscopy (EIS) measurements of the pure and functionalized polymers were carried out using a multichannel M204 potentiostat/galvanostat workstation equipped with an FRA 32 (Frequency Response Analyzer) over a frequency range of 0.1 Hz to 10^6 Hz. Thin films of the pure and functionalized polymers were sandwiched between two stainless steel circular electrodes with an effective area of 4.0 cm^2. The EIS analysis was performed to evaluate the electrical conductivity of the pure and functionalized polymers. The polymer resistance was obtained by fitting the impedance data using Nova software (version 2.1.4). The ionic conductivity of the polymers was then calculated from the measured ionic resistance using Equation (3).

$$\kappa^m = \frac{L\ (\text{cm})}{[R\ (\Omega)\ \times\ A\ (\text{cm}^2)]} \tag{3}$$

where, R is the resistance of the polymer, k^m is the ionic conductivity of the polymer, A is the area of the polymer, and L is the distance between the two electrodes.

2.7.7. Solar Cell Measurement

The Multichannel Autolab M204 potentiostat/galvanostat is used for the current-voltage (I–V) characterization of the fabricated QDSSC devices with an LED driver (700 mA output) and connected to an optical device. Illumination came from a focused LED light source powered by the Autolab LED driver. Programmable software (Nova 2.1.4) controlled the light intensity, which connected with the optical bench. The photovoltaic performance of the devices was evaluated by looking at the open-circuit voltage (V_{oc}), short-circuit current density (J_{sc}), and fill factor (FF). These parameters directly determine the power conversion efficiency (η). The following formulas were used to determine these parameters.

$$\text{FF} = \frac{J_{max}}{J_{sc}} \times \frac{V_{max}}{V_{oc}} \text{ or } \text{FF} = \frac{P_{max}}{J_{sc} \times V_{oc}}$$

$$\eta\ (\%) = \frac{P_{max}}{P_{in}} \times 100 \text{ or } \eta\ (\%) = \frac{J_{sc} \times V_{oc} \times \text{FF}}{P_{in}} \times 100$$

3. Results and Discussions

3.1. NMR, FTIR, UV-Vis, XRD, and DLS Analysis of Synthesized Polymers

Figure 1a Synthesis of polyurethane and introduction of sulfonate group into it is confirmed by ^1H and ^{13}C NMR studies, and the % (DS) degree of substitution of N–H proton by propane sultone is calculated through the selective integral area of the new incoming peak at 10.5 ppm, which corresponds to the $–SO_3H$ proton in ^1H-NMR spectra, as shown in Figure 1b. Before functionalization of Polyurethane, two different types of N–H protons were observed at 8.5 ppm (H_a) and 9.5 ppm (H_b), corresponding to the two types of urethane linkage present in the polymer backbone, which is also reflected in the ^{13}C NMR spectra. The aromatic reacting partner used in polyurethane synthesis was identified by a peak in the aromatic region at ~7.08 to ~7.33 ppm in ^1H NMR. Varying the condition of functionalization corresponds to a new peak intensity, which at 10.5 ppm ($–SO_3H$) varied, which reflects that the degree of substitution increases in the

case of SPU-2 than SPU-1, as supported by a N–H proton, which was found at 9.5 ppm and completely disappeared in the case of highly functionalized SPU-2. But the low degree of functionalization of SPU-1 resulted in a weak characteristic signal that was distinguishable only in the zoomed-in spectrum (Figure 1b). The proton of the alkyl chain of 1,3-Propane sultone was observed at 3.96 ppm, 1.43 ppm, and 1.20 ppm, confirming the functionalization [26,27].

In the ^{13}C NMR spectrum of PU and SPU, the urethane carbonyl carbon peaks, which appear at 162 ppm and 168 ppm in the case of unfunctionalized polyurethane, shifted to 167 ppm and 176 ppm after functionalization, as shown in Figure 1c. This deshielded behaviour was attributed to alkylation of the nitrogen atom in the urethane group. Also, peak shifting was observed in the case of aromatic carbons, which present around 115–130 ppm, which shifted to higher ppm, and a few new peaks came into the picture that belong to the alkyl chain of 1,3-Propane sultone, which are positioned at 28.5, 31.2, and 66.4 ppm, confirming the functionalization of polyurethane [28,29]. Equation (4) is used to calculate the degree of sulphonation.

$$\text{DS}\ (\%) = \frac{C}{\text{Aro} - H/2} \times 100 \tag{4}$$

where '*C*' is the peak area of the proton signal attributed to the SO_3–H group, and 'Aro–H' is the proton signal attributed to aromatic hydrogen. Based on these peak integrations, the degree of sulfonation was calculated to be 28% for SPU-1 and 64% for SPU-2. So, NMR studies confirm that SPU-2 shows higher substitution of the urethane N–H hydrogen atoms through sulphonate groups as compared to SPU-1.

Figure 1d shows the FTIR spectra of PU and SPU. Pure PU exhibits a characteristic absorption band at 3308 cm^{-1}, corresponding to the hydrogen-bonded >N–H group in the hard segment, which contributes to the stacking arrangement of the polymer. In contrast, the functionalized PU samples display broad bands at 3321 and 3348 cm^{-1} for SPU-1 and SPU-2, respectively, with the peak position progressively shifting to higher wavenumbers in SPU-2 as the degree of sulfonation increases, and this shifting occurs due to the stronger electron-withdrawing effect of the sulfonic group in the case of SPU-2 than that of SPU-1[30]. A new intense absorption band appears at 1174 cm^{-1} for SPU-1 and at 1181 cm^{-1} for SPU-2. This band is linked to the symmetric stretching vibration of the S=O group. The appearance of this band confirms the successful incorporation of sulfonate groups at different degrees of sulfonation within the polymer backbone. Notably, these absorption bands are absent in pristine PU. The gradual shift in the FTIR peak positions as sulfonation increases is due to the stronger electron-withdrawing effect of the sulfonic group and improved intermolecular hydrogen bonding between the sulfonate groups and the >NH moieties [31,32].

Figure 1e XRD analysis is conducted to investigate the crystallinity of the samples utilized in this study. The results indicate that aromatic moiety-based pure polyurethane exhibits an amorphous nature, showing a single diffuse peak at approximately 2θ = 21°, while SPU-1 and SPU-2 crystallinity is evident from the extra peak at approximately 25°, 28°, 31° in SPU-1 and 19°, 22°, 27°, 30.5°, 32°, 47° in SPU-2. However, SPU-2 is more crystalline than SPU-1, presumably due to a higher degree of sulphonation that results in stronger intermolecular hydrogen bonding between the sulfonic acid and urethane (–NH–COO–) groups [30,33].

Figure 1f shows the UV-visible absorption spectra of both pristine and functionalized PU samples. The pristine PU has an absorption peak at 295 nm, which relates to the $n \rightarrow \pi^*$ transition. In comparison, the functionalized polymers, SPU-1 and SPU-2, show broad absorption bands at 297 nm and 305 nm. These are primarily due to the sulfonate groups through the $n \rightarrow \pi^*$ transition [34]. Notably, another peak of pure PU at 358 nm and the functionalized PUs show at 364 nm SPU-1 and 368 nm SPU-2. In functionalized PU, the absorption peaks shift from pristine PU as sulfonation increases; the absorption peak progressively shifts toward a higher wavelength, indicating improved intermolecular interactions through specific interactions. The shift of the absorption edge toward the visible region at higher sulfonation levels also suggests a size quantization effect [35,36]. The optical band gap obtained from Tauc plots and the

corresponding energy level analysis are shown in Figure S1d. Overall, the spectroscopic results confirm successful sulfonation at different levels and demonstrate the potential of the functionalized PU as a promising material for solar cell applications.

The thermal stability of PU and functionalized PU was evaluated using thermogravimetric analysis (TGA), which monitors weight loss as a function of temperature. A two-step degradation pattern was observed for PU, SPU-1, and SPU-2. However, the functionalized PU (SPU-1) exhibited comparatively lower thermal stability as compared to SPU-2 due to the early decomposition of the sulfonate groups (Figure 1g). The breakdown of the hard segments of the polyurethane chains is responsible for the initial weight loss at lower temperatures, while the breakdown of the soft segments is responsible for the weight loss at higher temperatures. A slight weight loss at the initial stage in SPU-1 is associated with the evaporation of adsorbed moisture, which is due to the hydrophilic nature of the functionalized polyurethane [37]. The DSC thermograms of the synthesized polyurethane (PU) and sulphonated polyurethane (SPU), which are presented in Figure 1h. The pristine PU exhibited a broad thermal transition centered at approximately 43.6 °C, attributed to the melting of the PTMG-rich soft segment. Following sulphonation, the thermal transitions shifted towards higher temperatures. SPU-1 exhibited broad transitions at approximately 94 °C and 156.6 °C, while SPU-2 showed further shifts to around 114.66 °C and 186.3 °C. The rise in transition temperatures is attributed to the addition of sulfonic acid (–SO_3H) groups, which improve intermolecular hydrogen bonding, promote ionic aggregation, and restrict polymer chain mobility. Therefore, more thermal energy is needed to start segmental motion. The extensive temperature transitions originate from the heterogeneous microphase-separated structure of the segmented polyurethane and the unequal distribution of hydrogen-bonding contacts and sulfonic acid functionalities [38,39]. Overall, the DSC results show that the thermal rigidity of the polyurethane network and its intermolecular interactions improve with increasing degree of sulphonation.

The molecular properties and surface charge of the resulting prepolymer, polyurethane (PU), and sulphonated polyurethane (SPU-2) were characterized by dynamic light scattering (DLS) and zeta potential measurements using DMF as the dispersion medium, as shown in Figure 1i. The estimated molecular weight increased progressively from about 35 kDa for the prepolymer to 47 kDa for PU, and reached 67 kDa for SPU-2 [40]. The steady rise in molecular weight verifies successful chain extension during polyurethane synthesis, whereas the increasing molecular weight of SPU reveals the efficient insertion of sulphonate groups into the polymer backbone. SPU-2 seen somewhat higher apparent molecular weight, indicates that the addition of ionic functional groups improves polymer-solvent interactions in DMF, resulting in enhanced hydrodynamic volume and chain expansion. Additionally, the polymer network's intermolecular connections are strengthened by the presence of sulfonic acid groups and the hydrogen-bonding interactions that accompany them [41]. After chemical treatment, a consistent fluctuation was seen in the zeta potential data. The zeta potential of the prepolymer is −0.47, revealing a nearly neutral surface with few ionizable groups. For polyurethane, the zeta potential slightly shifts to a more negative value (−2.13), due to some rise in surface charge polarity by the addition of the sulphonic group. But in the case of SPU-2, a much larger negative zeta potential (−17.0 mV) was demonstrated, which happened because of the efficient insertion of sulphonate (–SO_3^-) groups into the polyurethane backbone, shown in Figure S1e and S1f. Since the DMF solvent is polar, so these highly acidic ionic groups dissolve, increasing the negative surface charge and improving the electrostatic stability of the polymer dispersion [42,43].

3.2. XRD, UV, FTIR, and TEM Analysis of Synthesized QDs

X-ray diffraction (XRD) was used to examine the phase purity and crystal structure of the synthesized $CuInS_2$ nanoparticles. The diffraction pattern of $CuInS_2$ is shown in Figure 2a. The distinct diffraction peaks were observed at 2θ values of 27.49° and 46.05°, which are consistent with the standard JCPDS card No. 85–1575, indicating the successful formation of crystalline $CuInS_2$ nanoparticles. The synthetic material's

nanocrystalline structure is evident in the broad shape of the diffraction peaks [44]. The Debye-Scherrer equation yielded an average crystallite size of 12.66 Å. These small-sized $CuInS_2$ QDs have a high surface-to-volume ratio, which underscores their potential as an effective absorber material for photovoltaic applications [45].

Figure 2b displays the synthesized $CuInS_2$ QDs' UV-vis absorption spectra. At 574 nm, a distinctive absorption peak is seen, which is in good agreement with values published in the literature [46]. While uncapped $CuInS_2$ quantum dots have been reported in literature to have an absorption band of around 512 nm [47]. The red shift of the absorption peak during DDT capping is attributed to a change in the surface electronic environment and improved surface passivation, which can reduce surface trap states and improve visible light absorption. The results suggest that the optical properties of $CuInS_2$ quantum dots can significantly be improved through DDT capping, indicating their potential applications in photovoltaic devices [34]. The optical band gap of $CuInS_2$ QDs is 1.78 eV, as calculated from Tauc's plots of the CIS QD absorption spectra, shown in Figure 2c.

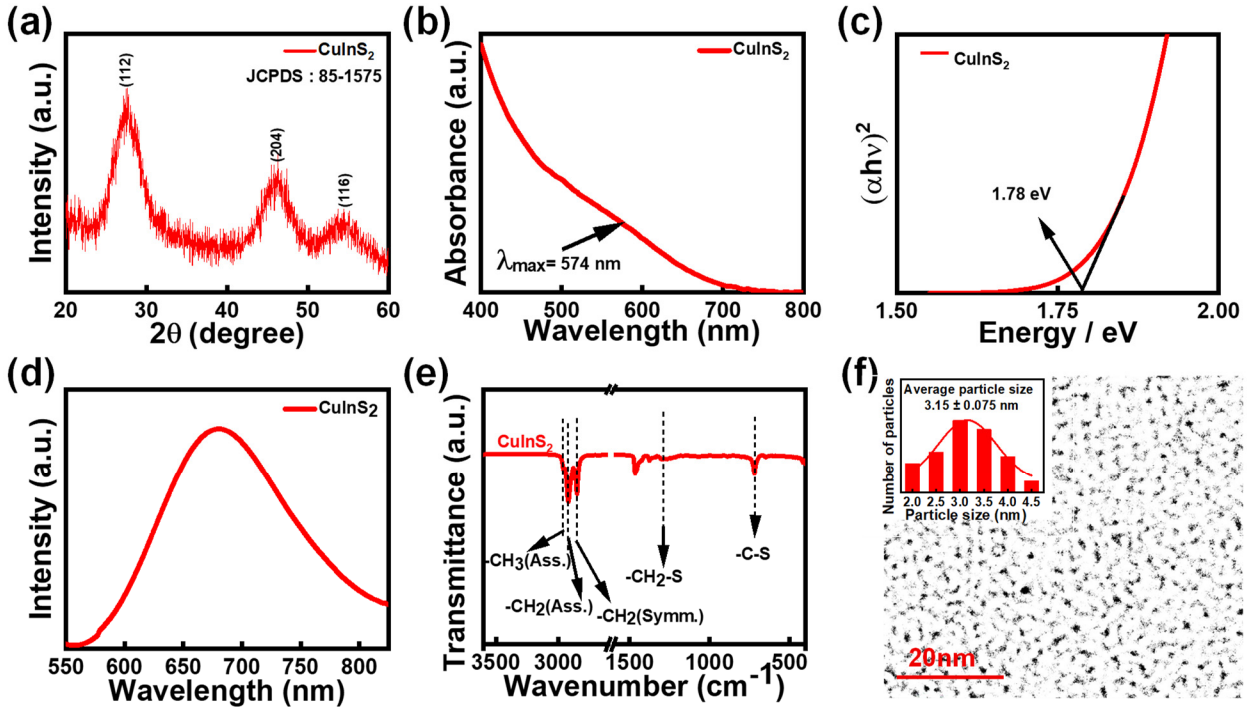

Figure 2. (**a**) Indicates the crystalline structure of $CuInS_2$ QDs; (**b**) UV-vis absorption spectra of $CuInS_2$ QDs; (**c**) optical band measurement of $CuInS_2$ QDs; (**d**) Photoluminescence (PL) spectrum of $CuInS_2$ QDs (at 680 nm); (**e**) FTIR spectra of the synthesized $CuInS_2$ QDs; (**f**) TEM image and particle size distribution histogram (inset) of $CuInS_2$ QDs.

Figure 2d shows the photoluminescence (PL) spectrum of the $CuInS_2$ QDs, revealing efficient radiative recombination of photoexcited charge carriers, with a strong, broad emission band at approximately 680 nm. The emission of $CuInS_2$ QDs at 680 nm is consistent with values reported in the literature [48].

The FTIR spectrum of the $CuInS_2$ quantum dots (QDs) capped with DDT is shown in Figure 2e. The spectra show three main absorption bands at 2968, 2925, and 2857 cm^{-1}. These bands correspond to the asymmetric stretching vibration of $–CH_3$, the asymmetric stretching vibration of $–CH_2$, and the symmetric stretching vibration of $–CH_2$, respectively. Moreover, the bands at 722 cm^{-1} are attributed to the wagging vibration of $–CH_2–S$, and those at 1292 cm^{-1} to the stretching vibration of C–S. The successful synthesis of DDT-capped $CuInS_2$ QDs is indicated by these characteristic vibrational bands, which confirm the presence of DDT as the surface ligand [34].

Figure 2f shows the TEM image of the synthesized $CuInS_2$ nanoparticles, which confirms the uniformly dispersed nanoparticles with almost spherical size and without agglomeration. The average particle size of $CuInS_2$ QDs is 3.15 nm (inset, Figure 2f), confirming the effective synthesis of ultrasmall $CuInS_2$ quantum dots with a limited size distribution. Their ultrasmall size gives a high surface-to-volume ratio, which is helpful for greater light harvesting, efficient charge transfer, and improved interfacial interactions, consequently making these nanoparticles suitable for photovoltaic and other optoelectronic applications [49,50].

3.3. Electrical Characterization of QDSSCs

3.3.1. Ionic Transport Nature of Pure Polymer and Functionalized Polymer

The electrical conductivity of the polymeric gel electrolytes has a significant impact on the photovoltaic performance of the fabricated devices. Therefore, the strong ionic conductivity of polymer electrolytes enables efficient hole transport during device operation. Electrochemical impedance spectroscopy (EIS) was used to assess the ionic conductivity of the synthesized polymers, and fitting and simulation techniques were applied to the associated Nyquist plots to determine the polarization resistance (Figures 3a and S1g). The resistance values of pure polyurethane, SPU-1, and SPU-2 films were found to be 5.1×10^6 Ω, 2.1×10^3 Ω, and 51 Ω, respectively. Using Equation (3), the ionic conductivities of pure polyurethane, SPU-1, and SPU-2 were calculated as 1.1×10^{-10} S·cm^{-1}, 4.76×10^{-6} S·cm^{-1}, and 3.7×10^{-4} S·cm^{-1}, respectively, as shown in Figure 3b. SPU-2 is appropriate as a hole transport layer for solar applications since its ionic conductivity is within the semiconducting range. This has happened because by adding ionizable sulfate groups creates mobile charge carriers and interconnected ionic pathways, thereby increasing polyurethane's ionic conductivity. It facilitates effective ion transport and lowers the polymer matrix's overall resistance [51,52].

3.3.2. Cyclic Voltammetry and Energy Profile Diagram

The HOMO and LUMO energy levels of functionalized polymer and ETLs, and the valence band (VB) and conduction band (CB) locations of the active layer (CIS QDs) were measured using cyclic voltammetry (CV). The oxidation onset potentials of SPU-2 and CIS QDs were recorded at 0.60 V and 0.85 V, respectively (Figure 3c,d). The HOMO energy levels of SPU-2 and CIS QDs were calculated to be −5.00 eV and −5.25 eV, respectively, using Equation (1) and the optical band gaps derived from the Tauc plots (Figures 2c and S1d). Based on the optical band gaps of SPU-2 (3.05 eV) and CIS QDs (1.78 eV), the corresponding LUMO energy levels were determined to be −1.95 eV and −3.47 eV, respectively (Figure 3g,h) [15,53]. Likewise, the reduction onset potentials of TiO_2 and SnO_2 were measured at −0.50 V and −0.26 V, respectively (Figure 3e,f). Applying Equation (2) and the optical band gaps derived from the Tauc plots (Figure S1h), the LUMO energy levels of TiO_2 and SnO_2 were calculated to be −3.9 eV and −4.2 eV, respectively. Their corresponding HOMO energy levels, obtained from the respective optical band gaps (TiO_2 is 3.28 eV and SnO_2 is 3.63 eV), were determined to be −7.18 eV and −7.83 eV, respectively [54,55], as illustrated in Figure 3g,h.

The energy band alignment suggests favorable hole transport in both Device-1 and Device-2. The valence band (VB) of the $CuInS_2$ quantum dots (QDs) is well aligned with the HOMO level of the polymer gel electrolyte, with a small energy offset of 0.25 eV, which promotes efficient hole extraction. In addition, the energy difference of 0.30 eV between the HOMO level of the gel electrolyte and the Ag counter electrode supports rapid hole transfer, thereby ensuring efficient hole transport in both devices [56].

In contrast, there are significant differences in the electron transport route. In Device-1, the energy difference between the TiO_2 LUMO and the FTO electrode is 0.50 eV, whereas the energy offset between the conduction band (CB) of the $CuInS_2$ QDs and the LUMO level of the TiO_2 electron transport layer (ETL) is 0.43 eV. These relatively high energy barriers make it difficult for electrons to be injected and transported, thereby increasing charge buildup, reducing photocurrent density, and eventually lowering

power conversion efficiency, as reflected in the case of Device-1 (Figure 3g) [57,58]. A more advantageous cascade energy-level alignment is established for Device-2 by adding a SnO_2 interlayer between the FTO substrate and TiO_2. The energy offset between the LUMO levels of TiO_2 and SnO_2 reduces to 0.30 eV, but the energy difference between SnO_2 and the FTO electrode is just 0.20 eV. By facilitating more effective electron transport from TiO_2 to SnO_2 and then to the FTO electrode, these lower energy barriers minimize charge recombination, enhance electron collecting, raise photocurrent density, and eventually provide a higher PCE than Device-1 (Figure 3h) [59].

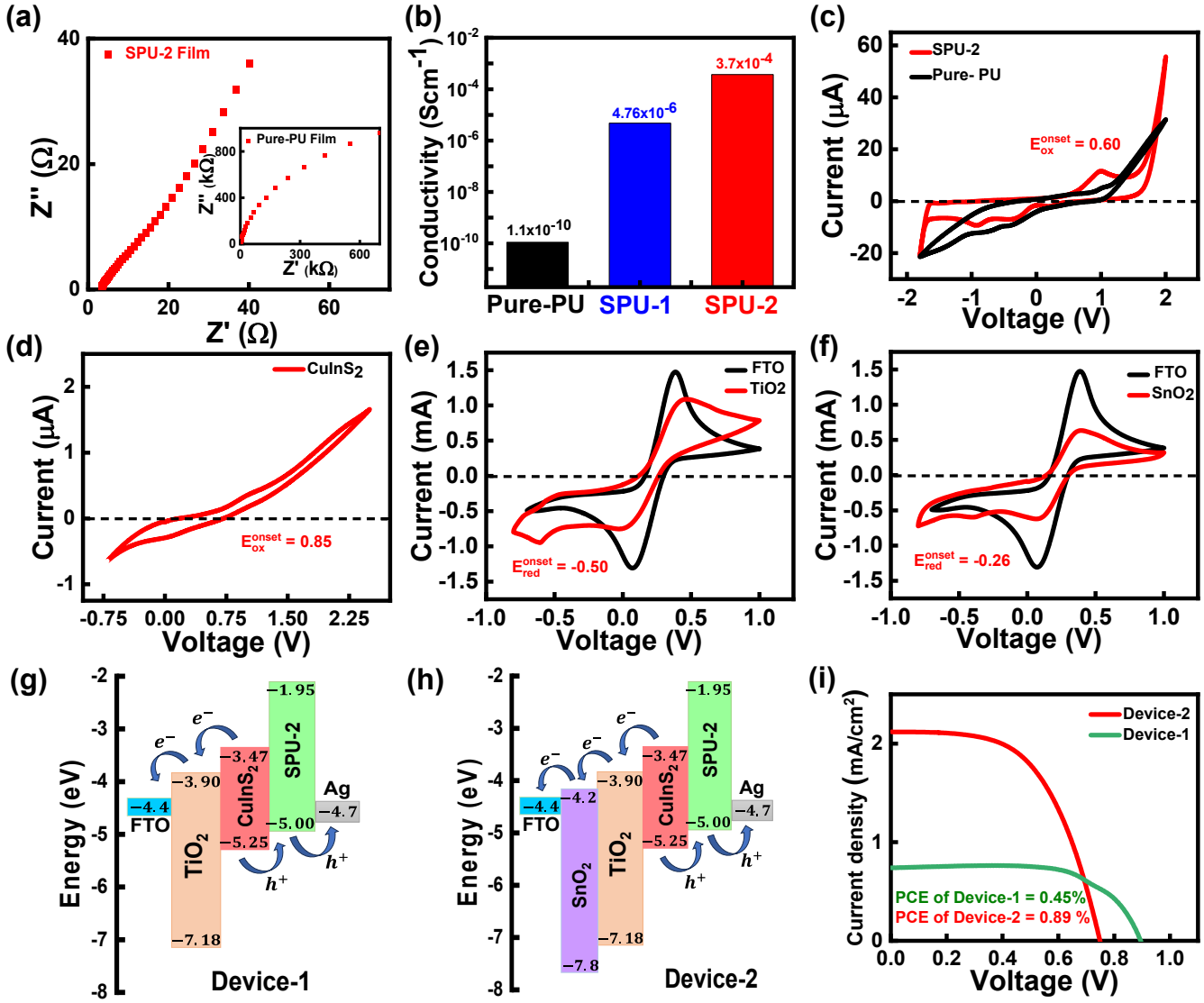

Figure 3. (**a**) Nyquist plots for SPU-2 and pure PU (inset); (**b**) histogram plot for ionic conductivity of pure-PU, SPU-1 and SPU-2 polymers; (**c**) CV measurement of indicated pure PU and SPU-2; (**d**) CV curve of $CuInS_2$ QDs; (**e**,**f**) CV curve of TiO_2 and SnO_2 film on FTO; (**g**,**h**) band diagram of Device-1 and Device-2; (**i**) *J-V* characteristic curve of Device-1 and Device-2.

3.3.3. Photovoltaic Performance

The *J–V* characteristics of the fabricated devices under standard AM 1.5G illumination appear in Figure 3i, and the corresponding photovoltaic parameters are summarized in Table 1 below. Device-1, which uses TiO_2 as ETL, delivers a PCE of 0.45%, along with FF of 67%, J_{sc} of 0.74 mA/cm^2, and V_{oc} of 0.89 V. But Device-2, by incorporating SnO_2/TiO_2 bilayer ETL, records higher performance, achieving a PCE of 0.89%, FF of 56%, J_{sc} of 2.12 mA/cm^2, and V_{oc} of 0.75 V. And the dark current of Device-1 and Device-2 is shown in Figure S1i.

Table 1. Experimental values of the different parameters of Device-1 and Device-2.

HTL	QDs	J_{sc} (mA/cm^2)	V_{oc} (V)	FF (%)	PCE (%)	Refs.
P3HT: PCBM	$CuInS_2$	4.48	0.539	34.7	0.84	[60]
PCBM	$CuInS_2$	1.69	0.46	46.3	0.36	[60]
PEDOT: PSS	$CuInS_2$	7.76×10^{-3}	0.62	22.7	0.0068	[61]
S_n^{2-}/S^{2-}	$CuInS_2$	9.87	0.57	48	2.61	[62]
S_n^{2-}/S^{2-}	$CuInS_2$	26.93	0.53	57	8.1	[63]
SPU-2	$CuInS_2$	0.74	0.89	67	0.45	This work (Device-1)
SPU-2	$CuInS_2$	2.12	0.75	56	0.89	This work (Device-2)

The incorporation of the SnO_2/TiO_2 bilayer ETL significantly increased the photocurrent density from 0.74 to 2.12 mA·cm^{-2}, due to enhanced electron extraction, higher electron mobility, and improved charge transport. Although the device exhibited a lower V_{oc} (0.75 V) and FF (56%), likely because of the lower conduction-band edge of SnO_2 and increased interfacial recombination at the SnO_2/TiO_2 interface, the marked improvement in J_{sc} outweighed these losses. Consequently, the power conversion efficiency nearly doubled from 0.45% to 0.89% [59,64]. Hence, by using SPU as HTL, the PCE of Device-1 and Device-2 is lower than that of the inorganic hole transport layers. Inorganic HTLs have higher charge mobility, better chemical stability, and greater resistance to heat and moisture [65]. However, when SPU is used as the HTL, PCE is comparable to or higher than that of several previously reported $CuInS_2$ QDSSCs that use polymeric hole transport layers.

4. Conclusions

The successful functionalization of PU is confirmed by ^{1}H NMR, FTIR, and UV-vis spectroscopy. Quantitative analysis of the ^{1}H NMR spectra, based on relative peak areas, revealed a maximum degree of sulfonation of 64%. The introduction of sulfonate groups into the PU resulted in a hydrophilic, electrically conductive ionomer, making it suitable for use as a polymer gel electrolyte in QDSSCs. The HOMO and LUMO energy levels of the gel electrolytes were systematically tuned by modulating the degree of sulfonation as obtained from cyclic voltammetry (CV) and optical band-gap measurements from UV-vis absorption spectroscopy. The increasing degree of functionalization also led to a higher melting temperature than pristine PU, which could be explained by stronger specific interactions between the sulfonate ionic groups and the urethane (>N–H) moieties along the polymer backbone.

The polymer gel electrolyte reduced electron back transfer and charge recombination at the surface while limiting electrolyte leakage and improving the built-in potential of the device. This led to notable high gains in open-circuit voltage and fill factor. Device-1 had a V_{oc} of 0.89 V and an FF of 67%. In contrast, Device-2 had a V_{oc} of 0.75 V and FF of 56%. To control nanocrystal growth and ensure colloidal stability, DDT was used as a capping agent during the synthesis of capping ligands, yielding $CuInS_2$ QDs with an average particle size of 3.15 nm. Device-1 used a TiO_2 electron transport layer (ETL), while Device-2 used a bilayer SnO_2/TiO_2 ETL. Using Tauc plot analyses and CV measurements, the energy band alignment of functionalized polymer gel electrolytes, $CuInS_2$ QD sensitizers and ETLs was investigated and an optimum energy level alignment diagram of the photoanode, the gel electrolyte, and the Ag counter electrode was constructed by appropriately tuning the size of the QDs, the PU functionalization and the ETL structure to study the electron and hole movement behaviour of electrons and holes.

For Device-2 (FTO/SnO_2/TiO_2/$CuInS_2$/SPU-2/Ag), by introduced a SnO_2/TiO_2 bilayer ETL between FTO and $CuInS_2$ ETL, which enhanced the photocurrent density from 0.74 mA·cm^{-2} (Device-1) to 2.12 mA·cm^{-2} owing to effective electron transport and extraction. Which led to a higher PCE value of 0.89% as compare to Device-1 (FTO/TiO_2/$CuInS_2$/SPU-2/Ag) PCE, 0.45%. Finally, these results indicated that

the functionalized polyurethane HTL, when used together with a SnO_2/TiO_2 bilayer ETL, can effectively promote charge transfer and enhance photovoltaic performance in $CuInS_2$-based QDSSCs.

Supplementary Materials

The following supporting information can be found at: https://www.sciepublish.com/article/pii/1188, Figure S1: (a) show digital photographs of unetched and etched FTO-coated glass; (b) digital photograph of Ag and TiO_2 coated FTO; (c) digital photograph of Device-1 and Device-2; (d) zetapotential graph of Pre-PU, PU, and SPU-2; (e) graph of relative frequency and zetapotential of Pre-PU, PU and SPU-2; (f) histogram of the zetapotential of Pre-PU, PU and SPU-2; (g) Nyquist plots for SPU-1; (h) UV-vis absorbance spectra and Tauc plot curve (inset) of TiO_2 and SnO_2; (i) Dark *I-V* curve of Device-1 & Device-2; Figure S2: (a) ^{1}H NMR spectra of PU; (b) ^{1}H NMR spectra of SPU-1 andSPU-2.

Acknowledgements

The authors are grateful to IIT (BHU) and its Central Instrument Facility; U.P. thanks IIT (BHU) for providing the PMRF fellowship (ID-1103081); A.K. is thankful to UGC, India, for providing the SRF; A.D. acknowledges the receipt of a research fellowship from the institute (IIT BHU).

Author Contributions

Conceptualization, P.M. and U.P.; Methodology, U.P.; Validation, U.P., S.K., A.K. and A.D.; Formal Analysis, U.P.; Investigation, U.P.; Data Curation, U.P.; Writing—Original Draft Preparation, U.P. and A.K.; Writing—Review & Editing, U.P. and P.M.; Visualization, U.P.; Supervision, P.M.

Ethics Statement

This study did not involve human participants, animals, or any biological samples requiring ethical approval.

Informed Consent Statement

This study did not involve human participants.

Data Availability Statement

The data presented in this study are available from the corresponding author upon reasonable request.

Funding

This research was funded by the Prime Minister's Research Fellowship (PMRF), Government of India.

Declaration of Competing Interest

The authors declare that they have no known competing financial interests or personal relationships that could have appeared to influence the work reported in this paper.

References

1. Yu Y, Ma T, Huang H. Semiconducting Quantum Dots for Energy Conversion and Storage. *Adv. Funct. Mater.* **2023**, *33*, 2213770. DOI:10.1002/adfm.202213770
2. Duan L, Hu L, Guan X, Lin C, Chu D, Huang S, et al. Quantum Dots for Photovoltaics: A Tale of Two Materials. *Adv. Energy Mater.* **2021**, *11*, 2100354. DOI:10.1002/aenm.202100354

3. Kokilavani S, Selopal GS. Advanced Surface Engineering and Passivation Strategies of Quantum Dots for Breaking Efficiency Barrier of Clean Energy Technologies: A Comprehensive Review. *Adv. Funct. Mater.* **2026**, *36*, e12718. DOI:10.1002/adfm.202512718
4. Buitrago E, Novello AM, Meyer T. Third-Generation Solar Cells: Toxicity and Risk of Exposure. *Helv. Chim. Acta.* **2020**, *103*, e2000074. DOI:10.1002/hlca.202000074
5. Gidwani B, Sahu V, Shukla SS, Pandey R, Joshi V, Jain VK, et al. Quantum dots: Prospectives, toxicity, advances and applications. *J. Drug Deliv. Sci. Technol.* **2021**, *61*, 102308. DOI:10.1016/j.jddst.2020.102308
6. Dong C, Liu R, Cao W, Meng W, Wang M. 6.56% Efficient $CuInS_2$ Superstrate Solar Cells Enabled by an Amorphous Tin Oxide Interlayer. *ACS Appl. Energy Mater.* **2026**, *9*, 2884–2891. DOI:10.1021/acsaem.6c00146
7. Peng Z, Gu Y, Li X, Lu B, Zhang X, Zhang Y, et al. High-Performance $CuInS_2$ Quantum Dot Sensitized Solar Cells Through I^-/MPA Dual-Ligands Passivation. *Chem. Asian J.* **2024**, *19*, e202400836. DOI:10.1002/asia.202400836
8. Shishodia S, Rinnert H, Balan L, Jasniewski J, Bruyère S, Medjahdi G, et al. Microwave-assisted synthesis of highly photoluminescent core/shell CuInZnSe/ZnS quantum dots as photovoltaic absorbers. *Nanoscale Adv.* **2025**, *7*, 1326–1334. DOI:10.1039/D4NA00893F
9. Peng Z, Sun Z, Chen J, Li W, Chen J, Liu Y, et al. Enhanced charge generation and transfer performance of the conical bamboo-like TiO_2 nanotube arrays photo-electrodes in quantum dot sensitized solar cells. *Sol. Energy* **2020**, *205*, 161–169. DOI:10.1016/j.solener.2020.05.026
10. Rahman A, Jennings JR, Khan MM. $CuInS_2$ and $CuInS_2$-based nanostructures as photocatalysts. *Mater. Sci. Semicond. Process.* **2024**, *169*, 107930. DOI:10.1016/j.mssp.2023.107930
11. Yoon N, Joo O, Chae S, Park E. Recent Advances in $CuInS_2$-Based Photocathodes for Photoelectrochemical H_2 Evolution. *Nanomaterials* **2023**, *13*, 1361. DOI:10.3390/nano13081361
12. Shilpa G, Kumar PM, Kumar DK, Deepthi PR, Sadhu V, Sukhdev A, et al. Recent advances in the development of high efficiency quantum dot sensitized solar cells (QDSSCs): A review. *Mater. Sci. Energy Technol.* **2023**, *6*, 533–546. DOI:10.1016/j.mset.2023.05.001
13. Guan S, Cao M, Jiao S, Ma R, Xi R, Hu C, et al. Dye-Sensitized Solar Cells With Quasi-Solid-State Electrolytes Based on Freeze-Dried Hydrogel Porous Structures. *ChemistrySelect* **2025**, *10*, e01854. DOI:10.1002/slct.202501854
14. Daems K, Yadav P, Dermenci KB, Van Mierlo J, Berecibar M. Advances in inorganic, polymer and composite electrolytes: Mechanisms of Lithium-ion transport and pathways to enhanced performance. *Renew. Sustain. Energy Rev.* **2024**, *191*, 114136. DOI:10.1016/j.rser.2023.114136
15. Kumar S, Maurya IC, Prakash O, Srivastava P, Das S, Maiti P. Functionalized Thermoplastic Polyurethane as Hole Conductor for Quantum Dot-Sensitized Solar Cell. *ACS Appl. Energy Mater.* **2018**, *1*, 4641–4650. DOI:10.1021/acsaem.8b00783
16. Kumar S, Maiti P. Review on Functional Electrolyte, Redox Polymers, and Solar Conversions in 3G Emerging Photovoltaic Technologies: Progress and Outlook. *Energy Fuels* **2023**, *37*, 14473–14511. DOI:10.1021/acs.energyfuels.3c01695
17. Ogundeji TS, Alamu GA, Oyewole OJ, Johnson MJ, Olaoye AO, Vyas S, et al. Review of recent progress in enhanced quantum dot solar cells via plasmonic nanostructures. *Next Mater.* **2026**, *11*, 101599. DOI:10.1016/j.nxmate.2026.101599.
18. Prakash R, Maiti P. Functionalized Thermoplastic Polyurethane Gel Electrolytes for Cosensitized TiO_2/CdS/CdSe Photoanode Solar Cells with High Efficiency. *Energy Fuels* **2020**, *34*, 16847–16857. DOI:10.1021/acs.energyfuels.0c03250
19. Li L, Pandey A, Werder DJ, Khanal BP, Pietryga JM, Klimov VI. Efficient Synthesis of Highly Luminescent Copper Indium Sulfide-Based Core/Shell Nanocrystals with Surprisingly Long-Lived Emission. *J. Am. Chem. Soc.* **2011**, *133*, 1176–1179. DOI:10.1021/ja108261h
20. Wang Z, Zhang X, Xin W, Yao D, Liu Y, Zhang L, et al. Facile Synthesis of Cu–In–S/ZnS Core/Shell Quantum Dots in 1-Dodecanethiol for Efficient Light-Emitting Diodes with an External Quantum Efficiency of 7.8%. *Chem. Mater.* **2018**, *30*, 8939–8947. DOI:10.1021/acs.chemmater.8b04282
21. Aldakov D, Sajjad MT, Ivanova V, Bansal AK, Park J, Reiss P, et al. Mercaptophosphonic acids as efficient linkers in quantum dot sensitized solar cells. *J. Mater. Chem. A* **2015**, *3*, 19050–19060. DOI:10.1039/C5TA04021C
22. Kumagai S, Motokucho S, Yabuki R, Anzai A, Kameda T, Watanabe A, et al. Effects of hard- and soft-segment composition on pyrolysis characteristics of MDI, BD, and PTMG-based polyurethane elastomers. *J. Anal. Appl. Pyrolysis* **2017**, *126*, 337–345. DOI:10.1016/j.jaap.2017.05.012
23. Santra A, Prakash R, Maity S, Nilawar S, Chatterjee K, Maiti P. Core–Shell Structure of Photopolymer-Grafted Polyurethane as a Controlled Drug Delivery Vehicle for Biomedical Application. *ACS Appl. Mater. Interfaces* **2024**, *16*, 17193–17207. DOI:10.1021/acsami.3c19155

24. Pramanik S, Chakraborty R, Maurya PP, Suman S, Swaminathan P, Pal BN. Oxide Memristor of Ag/Ag^+ Doped V_2O_5 and SnO_2 Bilayer Thin Film for Energy Efficient Memory, Logic and Neuromorphic Device Application. *Adv. Funct. Mater.* **2026**, *36*, e14732. DOI:10.1002/adfm.202514732
25. Peng S, Cheng F, Liang J, Tao Z, Chen J. Facile solution-controlled growth of $CuInS_2$ thin films on FTO and TiO_2/FTO glass substrates for photovoltaic application. *J. Alloys Compd.* **2009**, *481*, 786–791. DOI:10.1016/j.jallcom.2009.03.084
26. Parcheta P, Głowińska E, Datta J. Effect of bio-based components on the chemical structure, thermal stability and mechanical properties of green thermoplastic polyurethane elastomers. *Eur. Polym. J.* **2020**, *123*, 109422. DOI:10.1016/j.eurpolymj.2019.109422
27. Polo ML, Spontón ME, Jaramillo F, Estenoz DA, Meira GR. Linear segmented polyurethanes: I. A kinetics study. *J. Appl. Polym. Sci.* **2018**, *135*, 45747. DOI:10.1002/app.45747
28. Tang Q, Gao K. Structure analysis of polyether-based thermoplastic polyurethane elastomers by FTIR, ^{1}H NMR and ^{13}C NMR. *Int. J. Polym. Anal. Charact.* **2017**, *22*, 569–574. DOI:10.1080/1023666X.2017.1312754
29. Stefanović IS, Špírková M, Poręba R, Steinhart M, Ostojić S, Tešević V, et al. Study of the Properties of Urethane–Siloxane Copolymers Based on Poly(propylene oxide)-*b*-poly(dimethylsiloxane)-*b*-poly(propylene oxide) Soft Segments. *Ind. Eng. Chem. Res.* **2016**, *55*, 3960–3973. DOI:10.1021/acs.iecr.5b04975
30. Xiao Y, Huang H, Peng X. Synthesis of self-healing waterborne polyurethanes containing sulphonate groups. *RSC Adv.* **2017**, *7*, 20093–20100. DOI:10.1039/C6RA28416G
31. Bauri S, Tripathi S, Garg KA, Maiti P. Modulation of Drug Release: Exploring the Influence of Diisocyanate Variants on Polyurethane Matrix. *ACS Appl. Polym. Mater.* **2024**, *6*, 9499–9511. DOI:10.1021/acsapm.4c01231
32. Prakash R, Maurya IC, Srivastava P, Mondal S, Ray B, Maiti P. Functionalized polyurethane composite gel electrolyte with cosensitized photoanode for higher solar cell efficiency using a passivation layer. *Nanoscale Adv.* **2022**, *4*, 1199–1212. DOI:10.1039/D1NA00801C
33. Zhang M, Song X, Zhou C, Liu L, Wu G. Sulphonated hyperbranched wholly bio-based waterborne polyurethane sizing agents for strengthening the wettability and mechanical properties of carbon fibres. *Polymer* **2025**, *330*, 128510. DOI:10.1016/j.polymer.2025.128510
34. Prakash R, Das S, Maiti P. Non-toxic CuInS2 quantum dot sensitized solar cell with functionalized thermoplast polyurethane gel electrolytes. *Polymer* **2023**, *269*, 125708. DOI:10.1016/j.polymer.2023.125708
35. Erekath S, Kalpathy SK. Red-shifted optical absorption in films of azo-polyurea-polystyrene blends: Structural correlations and implications. *Opt. Mater.* **2022**, *126*, 112155. DOI:10.1016/j.optmat.2022.112155
36. Liu G, Zhang S, Xu L, Hu Y, Li X, Zhang S, et al. Recent advances of eco-friendly quantum dots light-emitting diodes for display. *Prog. Quantum Electron.* **2022**, *86*, 100415. DOI:10.1016/j.pquantelec.2022.100415
37. Ismoilov K, Akram W, Chauhan S, Ergasheva K, Artikboeva R, Islomova Z, et al. Synthesis and Evaluation of Properties of a Novel Cationic Waterborne Polyurethane Finishing Agent. *J. Chem. Eng. Process Technol.* **2019**, *10*, 398. DOI:10.35248/2157-7048.19.10.398
38. Luo YL, Gao WT, Luo ZY, Li CH. Toward mechanically robust self-healing polyurethanes using dynamics chemistry. *Mater. Chem. Front.* **2024**, *8*, 1767–1791. DOI:10.1039/D3QM01251D
39. Wu HC, Shao SR, Dong SH, Wang A, Li Z, Han XL, et al. Influence of Hydrogen Bonding on the Temperature-Accelerated Hydrolysis of Silicone Based Polyetherurethane. *Chin. J. Polym. Sci.* **2023**, *41*, 1230–1237. DOI:10.1007/s10118-023-2957-8
40. Mandal SS, Choudhury AM, Gupta A, Maiti P. An injectable cyclodextrin extended polyurethane/carboxymethyl cellulose hydrogel for controlled release of insulin: *In-vitro* and *in-vivo* diabetic animal model study. *Carbohydr. Polym.* **2025**, *356*, 123396. DOI:10.1016/j.carbpol.2025.123396
41. Puskás I, Szemjonov A, Fenyvesi É, Malanga M, Szente L. Aspects of determining the molecular weight of cyclodextrin polymers and oligomers by static light scattering. *Carbohydr. Polym.* **2013**, *94*, 124–128. DOI:10.1016/j.carbpol.2013.01.025
42. Zhang J, Lv S, Zhao X, Ma S, Zhou F. Functional Zwitterionic Polyurethanes: State-of-the-Art Review. *Macromol. Rapid Commun.* **2024**, *45*, 2300606. DOI:10.1002/marc.202300606
43. Zhang J, Lv S, Zhao X, Ma S, Zhou F. Surface functionalization of polyurethanes: A critical review. *Adv. Colloid Interface Sci.* **2024**, *325*, 103100. DOI:10.1016/j.cis.2024.103100
44. Lu SH, Chen TF, Wang AJ, Zheng D, Li YL, Wang YS. Modulation of structures of $CuInS_2$ nanoparticles grown with ethylxanthate salts. *Mater. Sci. Eng. B* **2016**, *203*, 19–26. DOI:10.1016/j.mseb.2015.09.001
45. Dong X, Ren J, Li T, Wang Y. Synthesis, characterization and application of red-emitting $CuInS_2$/ZnS quantum dots for warm white light-emitting diodes. *Dye. Pigment.* **2019**, *165*, 273–278. DOI:10.1016/j.dyepig.2019.02.035

46. Nam DE, Song WS, Yang H. Noninjection, one-pot synthesis of Cu-deficient $CuInS_2$/ZnS core/shell quantum dots and their fluorescent properties. *J. Colloid Interface Sci.* **2011**, *361*, 491–496. DOI:10.1016/j.jcis.2011.05.058
47. Richardson A, Alster J, Khoroshyy P, Psencik J, Valenta J, Tuma R, et al. Direct Synthesis and Characterization of Hydrophilic Cu-Deficient Copper Indium Sulfide Quantum Dots. *ACS Omega* **2024**, *9*, 17114–17124. DOI:10.1021/acsomega.3c09531
48. Wu Q, Cai C, Zhai L, Wang J, Kong F, Yang Y, et al. Zinc dopant inspired enhancement of electron injection for $CuInS_2$ quantum dot-sensitized solar cells. *RSC Adv.* **2017**, *7*, 39443–39451. DOI:10.1039/C7RA06659G
49. Alayeto I, Gutierrez-Gonzalez P, Dongmei Q, Pallarés Vilar A, Hamraoui K, Civera C, et al. Ion-Mediated Photoluminescence Enhancement in $CuInS_2$ Quantum Dots and Its Use as Heavy Metal Ion Sensor. *ACS Appl. Nano Mater.* **2025**, *8*, 14461–14469. DOI:10.1021/acsanm.5c02927
50. Yan R, Zhang W, Wu W, Dong X, Wang Q, Fan J. Optical spectroscopy reveals transition of $CuInS_2$/ZnS to $Cu_xZn_{1-x}InS_2$/ZnS:Cu alloyed quantum dots with resultant double-defect luminescence. *APL Mater.* **2016**, *4*, 126101. DOI:10.1063/1.4971353
51. Yu Y, Zeng Z, Gao X, Xiong C, Zhu H, Cen H, et al. A Maximization of the Proton Conductivity of Sulfonated Poly(Ether Ether Ketone) with Grafted Segments Containing Multiple, Flexible Propanesulfonic Acid Groups. *Macromol. Rapid Commun.* **2023**, *44* ,2200926. DOI:10.1002/marc.202200926
52. Li X, He B, Li P, Tang S. In Situ-Doped Sulfonated Schiff-Base Networks in SPEEK Composite Membranes with Enhanced Proton Conductivity. *ACS Appl. Mater. Interfaces* **2023**, *15*, 25584–25593. DOI:10.1021/acsami.3c03885
53. Tithito T, Kondee S, Seekaew Y, Traiwatcharanon P, Chaloeipote G, Seesaard T, et al. $CuInS_2$ quantum dots-based electrochemical sensor for indole detection. *J. Alloys Compd.* **2026**, *1062*, 187552. DOI:10.1016/j.jallcom.2026.187552
54. Milinković E, Cvetanović K, Bošković MV, Conić N, Jovanov V, Stanisavljev D, et al. The Comprehensive Study of TiO_2 Blocking Layer with Complementary Electrochemical and SPM Methods for the Application in Photovoltaics. *Inorganics* **2025**, *13*, 270. DOI:10.3390/inorganics13080270
55. Raj DV, Ponpandian N, Viswanathan C. Electrodeposition of SnO_2 nanostructures onto copper substrates and their electrochemical properties. *Mater. Sci. Technol.* **2023**, *39*, 1414–1424. DOI:10.1080/02670836.2023.2171766
56. Bertens K, Fan JZ, Biondi M, Rasouli AS, Lee S, Li P, et al. Colloidal Quantum Dot Solar Cell Band Alignment using Two-Step Ionic Doping. *ACS Mater. Lett.* **2020**, *2*, 1583–1589. DOI:10.1021/acsmaterialslett.0c00379
57. Deo M, Möllmann A, Haddad J, Ünlü F, Kulkarni A, Liu M, et al. Tantalum Oxide as an Efficient Alternative Electron Transporting Layer for Perovskite Solar Cells. *Nanomaterials* **2022**, *12*, 780. DOI:10.3390/nano12050780
58. Krishna BG, Ghosh DS, Tiwari S. Hole and electron transport materials: A review on recent progress in organic charge transport materials for efficient, stable, and scalable perovskite solar cells. *Chem. Inorg. Mater.* **2023**, *1*, 100026. DOI:10.1016/j.cinorg.2023.100026
59. Patel U, Kumar A, Pramanik S, Devi A, Pal BN, Maiti P. SnO_2 as Electron Transport Layer in $CsPbBr_3$ Perovskite Solar Cells: Experimental and Simulation Approaches. *ACS Appl. Energy Mater.* **2026**, *9*, 593–605. DOI:10.1021/acsaem.5c03357
60. Liu M, Yan N, Zhang C, Li L. Integrated solar cells with non-toxic inorganic nanocrystals and polymer bulk heterojunction. *Appl. Surf. Sci. Adv.* **2021**, *3*, 100052. DOI:10.1016/j.apsadv.2020.100052
61. Yue W, Han S, Peng R, Shen W, Geng H, Wu F, et al. $CuInS_2$ quantum dots synthesized by a solvothermal route and their application as effective electron acceptors for hybrid solar cells. *J. Mater. Chem.* **2010**, *20*, 7570. DOI:10.1039/c0jm00611d
62. Karkhaneh A, Marandi M. Modified synthesis of $CuInS_2$ nanoparticles for enhancement of the efficiency of corresponding quantum dot-sensitized solar cells: A simplified aqueous approach. *Emergent Mater.* **2025**, *8*, 3529–3543. DOI:10.1007/s42247-024-00987-5
63. Du Z, Ma D. Recent progress in I-III-VI colloidal quantum dots-integrated solar cells. *Curr. Opin. Colloid Interface Sci.* **2025**, *75*, 101890. DOI:10.1016/j.cocis.2024.101890
64. Du B, He K, Tian G, Che X, Song L. Robust electron transport layers of SnO_2 for efficient perovskite solar cells: Recent advances and perspectives. *J. Mater. Chem. C* **2023**, *11*, 13625–13646. DOI:10.1039/D3TC02445H
65. Cai X, Hu T, Hou H, Zhu P, Liu R, Peng J, et al. A review for nickel oxide hole transport layer and its application in halide perovskite solar cells. *Mater. Today Sustain.* **2023**, *23*, 100438. DOI:10.1016/j.mtsust.2023.100438